JGR Space Physics

RESEARCH ARTICLE
10.1029/2018JA026184

Contribution of ULF Wave Activity to the Global Recovery of the Outer Radiation Belt During the Passage of a High-Speed Solar Wind Stream Observed in September 2014

L. A. Da Silva[1,2], D. Sibeck[3], L. R. Alves[2], V. M. Souza[2], P. R. Jauer[1,2], S. G. Claudepierre[4], J. P. Marchezi[2,3], O. Agapitov[5], C. Medeiros[2], L. E. A. Vieira[2], C. Wang[1], S. Jiankui[1], Z. Liu[1], W. Gonzalez[2], A. Dal Lago[2], M. Rockenbach[2], M. B. Padua[2], M. V. Alves[2], M. V. G. Barbosa[2], M.-C. Fok[3], D. Baker[6], C. Kletzing[7], S. G. Kanekal[3], and M. Georgiou[8,9]

[1]State Key Laboratory of Space Weather, National Space Science Center, Chinese Academy of Sciences, Beijing, China, [2]Instituto Nacional de Pesquisas Espaciais, São José dos Campos, Brazil, [3]NASA Goddard Space Flight Center, Greenbelt, MD, USA, [4]The Aerospace Corporation, Los Angeles, CA, USA, [5]Space Science Laboratory, University of California, Berkeley, CA, USA, [6]Laboratory for Atmosphere and Space Physics, Boulder, CO, USA, [7]Department of Physics and Astronomy, University of Iowa, Iowa City, IA, USA, [8]Mullard Space Science Laboratory, University College London, Dorking, UK, [9]Department of Physics, National and Kapodistrian University of Athens, Zografos, Greece

Abstract Energy coupling between the solar wind and the Earth's magnetosphere can affect the electron population in the outer radiation belt. However, the precise role of different internal and external mechanisms that leads to changes of the relativistic electron population is not entirely known. This paper describes how ultralow frequency (ULF) wave activity during the passage of Alfvénic solar wind streams contributes to the global recovery of the relativistic electron population in the outer radiation belt. To investigate the contribution of the ULF waves, we searched the Van Allen Probes data for a period in which we can clearly distinguish the enhancement of electron fluxes from the background. We found that the global recovery that started on 22 September 2014, which coincides with the corotating interaction region preceding a high-speed stream and the occurrence of persistent substorm activity, provides an excellent scenario to explore the contribution of ULF waves. To support our analyses, we employed ground- and space-based observational data and global magnetohydrodynamic simulations and calculated the ULF wave radial diffusion coefficients employing an empirical model. Observations show a gradual increase of electron fluxes in the outer radiation belt and a concomitant enhancement of ULF activity that spreads from higher to lower L-shells. Magnetohydrodynamic simulation results agree with observed ULF wave activity in the magnetotail, which leads to both fast and Alfvén modes in the magnetospheric nightside sector. The observations agree with the empirical model and are confirmed by phase space density calculations for this global recovery period.

Key Points:
- ULF waves reached the lowest magnetospheric L-shells at the end of the period on 24 September
- Relativistic electron population reached the lowest magnetospheric L-shells at the end of the period on 24 September
- Enhancement of the electron flux occurs concomitantly with the Alfvénic fluctuations following a solar wind sector boundary crossing

Supporting Information:
- Supporting Information S1

Correspondence to:
L. A. Da Silva,
ligia.alves01@gmail.com;
ligia.silva@inpe.br

Citation:
Da Silva, L. A., Sibeck, D., Alves, L. R., Souza, V. M., Jauer, P. R., Claudepierre, S. G., et al. (2019). Contribution of ULF wave activity to the global recovery of the outer radiation belt during the passage of a high-speed solar wind stream observed in September 2014. *Journal of Geophysical Research: Space Physics*, *124*, 1660–1678. https://doi.org/10.1029/2018JA026184

Received 14 OCT 2018
Accepted 19 FEB 2019
Accepted article online 22 FEB 2019
Published online 18 MAR 2019

1. Introduction

Outer radiation belt electrons trapped within the Earth's magnetic field undergo a complex periodic motion that can vary adiabatically. The particle motion can be understood as a combination of gyromotion around the magnetic field lines, bounce motion wherein particles mirror back and forth between the magnetic mirror points, and an azimuthal drift at fixed L-shells (Northrop & Teller, 1960; Roederer, 1970; Shabansky, 1971; Ukhorskiy & Sitnov, 2013). Due to the variety of electrodynamic processes in the magnetosphere, violations of the adiabatic invariants associated with each of the three motions can occur, causing electrons to be accelerated or scattered from the radiation belts that result in decreased fluxes (Baker et al., 1994; Baker & Kanekal, 2008; Blake et al., 1992). The population of the outer radiation belt electron flux may decrease (see Alves et al., 2016, and references therein) or increase (Artemyev et al., 2013; Baker et al., 2014; Bortnik & Thorne, 2007; Potapov, 2013; Thorne, 2010; Thorne et al., 2013; Turner et al., 2013), relative to background levels, according to the electromagnetic process involved, such as wave-particle interactions mediated by waves either in the ultralow frequency (ULF) range (a few milihertz up to a about 5 Hz; Cahill & Winckler, 1992; Kivelson & Southwood, 1985; Mann et al., 1999) or in higher-

frequency ranges like the whistler mode chorus waves in the few hundreds of hertz to a few tens of kilohertz (Gurnett & O'Brien, 1964). This work investigates the role of ULF wave-driven radial diffusion mechanism on electron flux enhancement from 22 to 24 September 2014, when the Earth was under the influence of a high solar wind speed stream (HSS).

The Earth's magnetosphere is embedded in the highly variable interplanetary extension of the outer layers of the solar atmosphere, the solar wind (Hundhausen, 1972, 1995). In situ observations of the solar wind plasma conditions and magnetic field show that during periods of low solar activity (solar minima) the slow solar wind (~350 km/s) is confined to the low-latitude regions of the Sun, while the fast solar wind (~600 km/s) is observed at higher latitudes (Krieger et al., 1973). During periods of high solar activity (solar maxima), the configuration of the solar magnetic field departs significantly from the quasi-dipolar configuration observed during solar minima. Therefore, the global structure of the solar wind changes, reflecting the structure of the solar atmosphere near the solar surface (Balogh et al., 1999). During solar maximum and the descending phase of solar activity the fast solar wind can extend to low latitudes. The coupling between the fast and slow wind results in the evolution of a corotating interaction region (Sheeley et al., 1976Tsurutani et al., 2006). Superimposed on the global structure of the solar wind, transients are more frequently observed during solar maxima. Most of these transients are the interplanetary counterparts of coronal mass ejections (Echer et al., 2011Gosling, 1990).

Coupling between the solar wind and the Earth's magnetosphere depends on the global structure of the solar wind, including interplanetary coronal mass ejections. Previous studies have shown that there is a relationship between the properties of the solar wind during HSS and the dynamics of electron fluxes in the outer radiation belt (Hendry et al., 2012; MacDonald et al., 2010; Ogunjobi et al., 2017). Here we investigate the impact of the high-speed and low-density solar wind streams on the acceleration of high-energy electrons trapped in the outer radiation belt (e.g., Li et al., 2015). We point out that during the passage of the HSS a large amount of energy can be transferred to the magnetosphere (Baker et al., 1990, 1997; Paulikas & Blake, 1979; Potapov, 2013). The interplanetary magnetic field (IMF) components are analyzed to identify the degree to which Alfvénic fluctuations are present and to verify the possibility of initiating reconnection with the Earth's magnetic field, which allows the solar wind energy to be transported into the magnetosphere. Additionally, we process the Van Allen Probes data and estimate numerically the effects of ULF wave power spectral density (PSD) on the outer radiation belt, highlighting the intensity, depth, and preferential polarization modes of the excited ULF waves. We estimate, through an empirical model (Ozeke et al., 2014), the ULF wave's radial diffusion coefficient D_{LL} to quantify the contribution of these waves to the global recovery. Finally, phase space density (PhSD) is calculated as a function of the three adiabatic invariants that constrain the electron motion: μ, K, and L^* parameter (Roederer, 1970). Inspection of the radial gradient of PhSD versus L^* enables us to identify the main dynamic mechanisms, including the effects of inward radial diffusion driven by ULF waves during the global recovery of the outer belt electron fluxes.

2. Instrumentation

We employ Relativistic Electron-Proton Telescope (REPT; Baker et al., 2013) observations from Van Allen Probe A (Mauk et al., 2012) to study radiation belt electron intensities. The Magnetic Field Experiment (MAG) and Solar Wind Electron, Proton and Alpha Monitor (SWEPAM) on board the Advanced Composition Explorer (ACE) provides solar wind parameters at the L1 Lagrangian point (Stone et al., 1998).

The ULF wave PSD used in this study was calculated from the International Monitor for Auroral Geomagnetic Effects (IMAGE) ground magnetometer network (Viljanen & Hakkinen, 1997) and the Electric and Magnetic Field Instrument Suite and Integrated Science (EMFISIS) (Kletzing et al., 2013) and Electric Field and Waves (EFW; Wygant et al., 2013) instruments on board the Van Allen Probes.

3. Description of the Solar Wind Conditions and the Time-Evolution of the High-Energy Electron Flux

Figure 1 presents the conditions within the Earth's radiation belt and solar wind from 10 to 25 September 2014. Particularly, the panels present the following: (a) REPT observations of the relativistic (2.10 MeV) omnidirectional (i.e., averaged over all 17 pitch angle bins) electron flux as a function of time and the L^* parameter, which is commonly referred to as Roederer L related to the third adiabatic invariant

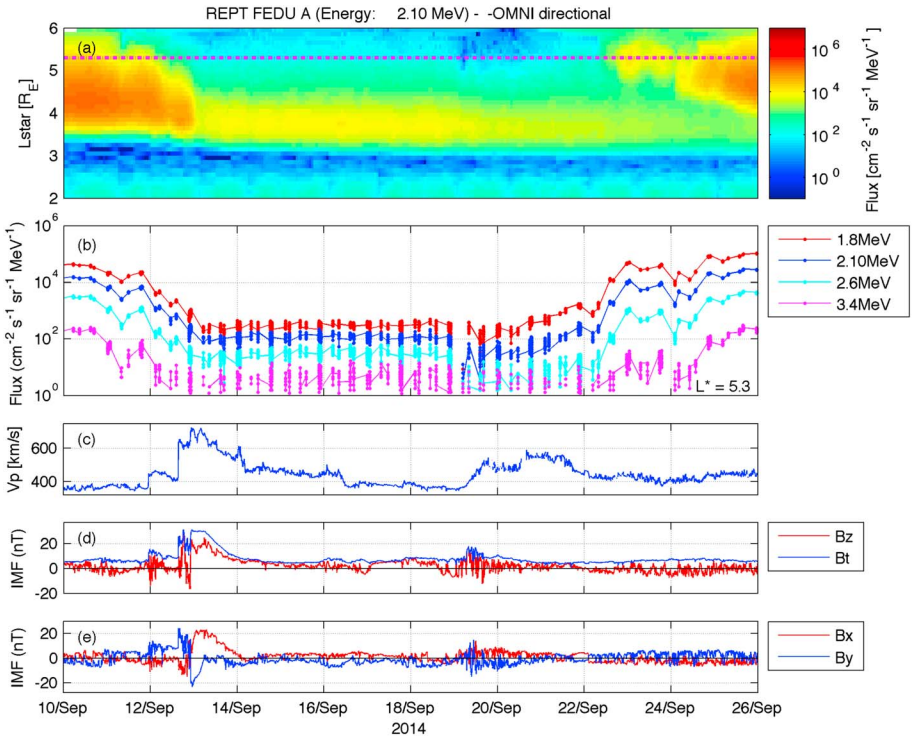

Figure 1. (a) Electron flux at 2.10-MeV energy as a function of L^* (vertical axis) and time (horizontal axis); (b) electron fluxes at 1.8-, 2.10-, 2.6-, and 3.4-MeV energies at a fixed $L^* = 5.3\ R_E$ location; (c) solar wind speed (Vp); (d) Interplanetary magnetic field (IMF) intensity (Bt) and Bz component of the IMF; and (e) Bx component and By component of the IMF. The electron fluxes are obtained by the Relativistic Electron-Proton Telescope (REPT) instrument on board of the Van Allen Probes. The Vp, Bt, Bz, Bx, and By are obtained by the Advanced Composition Explorer (ACE) satellite in the Lagrangian L1 point.

(Roederer, 1970); (b) REPT's observations of the fluxes within its lowest four electron energy channels acquired at a fixed L^* (~5.3 R_E); and the solar wind parameters observed at the L1 Lagrangian point, namely, (c) the solar wind speed, (d) IMF magnitude and the north-south (Bz) component, and (e) the IMF Bx and By components in geocentric solar magnetosphere coordinates.

At the beginning of the period shown, particularly between 11 and 15 September, the Earth's magnetosphere was embedded in a complex solar wind structure resulting from the interaction of a sequence of two interplanetary coronal mass ejections. The outer Van Allen radiation belt electron flux was severely depleted on 12 September (cf., e.g., Alves et al., 2016; Jaynes et al., 2015), followed by a 10-day-long quiescent period (see Ozeke et al., 2017). On early 19 September, the electron flux at the outskirts of the outer belt, that is, at $L^* > \sim 5\ R_E$, was further diminished due to a corotating interaction region that reached the Earth's magnetosphere. The solar wind speed (Figure 1c) increased in two steps, first reaching ~ 490 to ~ 500 km/s late on 19 September and maintaining such high values up to midday on 20 September, followed by a second enhancement in which the solar wind speed plateaued around ~ 550 km/s until around midday on 21 September, when it started to decrease back to typical values. During the first and second solar wind speed increases, Van Allen Probe A detected only minor relativistic electron flux changes, most notably in the lowest two REPT's energy channels. It is only from 22 September onward that the outer belt electron flux increased significantly, within ~ 14 hr, as seen in Figures 1a and 1b). For this reason, this work will focus from this date. The flux change coincided with two IMF features: (i) a southward turning of the Bz component from an average $Bz > 0$ to an average $Bz < 0$ orientation and (ii) a sector boundary crossing with reversals in Bx and By, as seen respectively in Figures 2c and 2d, which shows part of the time interval in Figure 1 with greater resolution. From 23 September onward, the three IMF components fluctuated greatly. Close inspection (Figures 2b and S1 in the supporting information) shows that such fluctuations are mostly Alfvénic in nature, and during this period the outer belt electron flux was further enhanced.

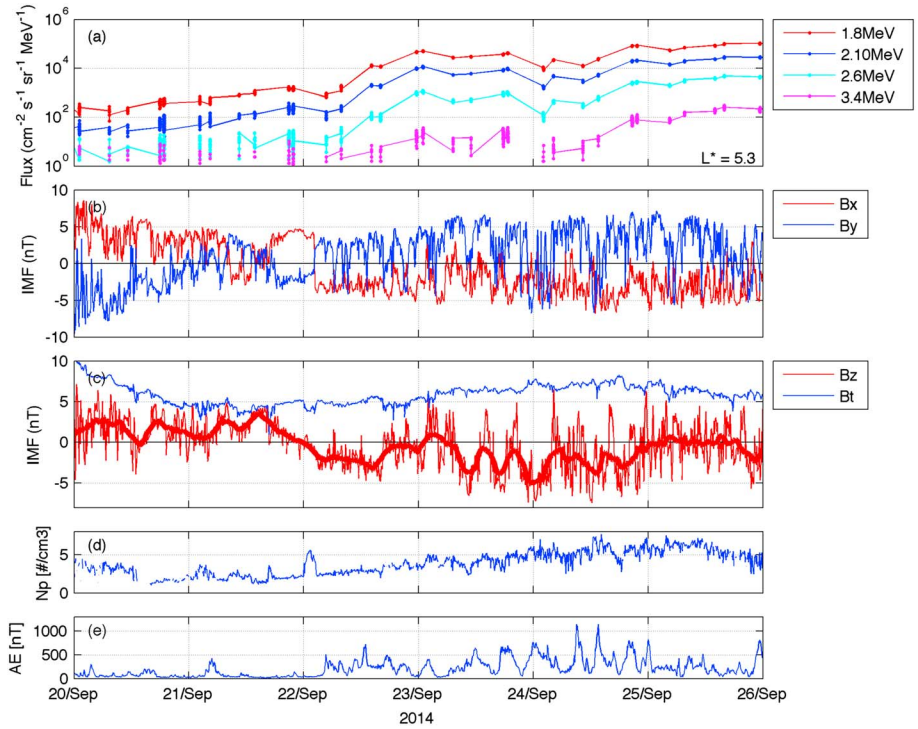

Figure 2. (a) The electron fluxes 1.8, 2.10, 2.6, and 3.4 MeV to *L** 5.3; (b) *Bx* component and *By* component of the interplanetary magnetic field (IMF); (c) the IMF intensity (*Bt*) and *Bz* component of the IMF (solid red line represents a 4-hr running average); (d) solar wind density (*Np*); (e) geomagnetic auroral electrojet [*AE*] index. The electron fluxes are obtained by the Relativistic Electron-Proton Telescope instrument on board of the Van Allen Probe A. The *Np*, *Bt*, *Bz*, *Bx*, and *By* are obtained by the Advanced Composition Explorer satellite in the Lagrangian L1 point. *AE* index is obtained from the World Data Center for Geomagnetism, Kyoto.

Alfvénic fluctuations in the solar wind are the signature of coronal plasma transported toward the Earth (Belcher & Davis, 1971; Cranmer & van Ballegooijen, 2005; Goldstein et al., 1995; Morton et al., 2015; Tu & Marsch, 1995). Low-frequency solar wind Alfvénic fluctuations (Lee et al., 2006; Zhang et al., 2014) that provide prolonged intervals of southward *Bz* (Gonzalez et al., 1994) can initiate reconnection on the Earth's dayside magnetopause, which allows solar wind energy to enter the magnetosphere and drive moderate-intensity geomagnetic storms (Tsurutani et al., 1995) and recurrent substorms. The arrival of such solar wind structures can also generate a wide range of magnetospheric oscillation frequencies, among them, the ULF wave modes, which are recognized as efficient accelerators of the seed population particles responsible for the outer radiation belt global recovery (Summers et al., 2002; Horne & Thorne, 2003; Thorne et al., 2005; Elkington, 2006; Elkington et al., 1999; Summers & Ma, 2000; Perry et al., 2005, Ozeke et al., 2014 and others). James et al. (2013) performed a statistical analysis of 83 substorm events, and they showed that substorm activity can function as an internal (i.e., within the Earth's magnetosphere) source of poloidal-mode (high-*m*) ULF waves. On the other hand, James et al. (2015) analyzed three individual substorm events and showed that the magnetospheric ULF waves can be driven by sources both internal and external to the magnetosphere. They suggested that the waves driven by energy sources external to the magnetosphere (e.g., Kelvin-Helmholtz instability on the magnetopause or solar wind buffeting) are often characterized by low azimuthal wave numbers (*m*) or large azimuthal scale sizes.

Inspection of Figure 2 during the global electron flux recovery event from 22 September onward shows that the solar wind features commonly associated with ULF wave generation in the magnetosphere, such as enhanced speeds and/or densities, are absent. During this period we only see a change in the heliospheric current sheet sector, which is accompanied by substorm activity (see *AE* index in Figure 2e and Pi2 activity in Figure S2 in the supporting information) and the presence of an on average southward IMF *Bz* (thick line on Figure 2c) and IMF Alfvénic fluctuations.

IMF observations on 22 September indicate the presence of Alfvénic fluctuations (Figure S1). The IMF *Bz* component was preferentially southward (Figures 1d and 2c), conducive to magnetospheric substorm activity (Figures 2e and S2). According to Jaynes et al. (2015), substorms were a crucial element for the injection of low-energy electrons in the outer radiation belt on this day. They suggested a scheme based on substorm injection and very low frequency (VLF) waves to explain the relativistic acceleration mechanism in the Earth's magnetosphere. In their scheme, the source population (tens of keV) is injected via substorms, resulting in unstable particle distributions that in turn generate VLF waves. Interaction with these VLF waves energizes the seed populations to relativistic energies (hundreds of keV). Jaynes et al. (2015) noted the presence and possible importance of ULF waves during this interval but did not provide a full explanation of the role they play. We will investigate the effects/role/contribution of ULF wave-particle interactions during the enhancement of the high-energy electron flux in the outer radiation belt observed in this event. We then argue that for the global recovery event being analyzed here, the conjunction of IMF *Bz* and IMF Alfvénic fluctuations along with the presence of substorms play an important role in generating both the compressional and toroidal ULF wave modes.

4. ULF Waves Activity in the Magnetosphere

According to the description in section 3, the solar wind can drive ULF waves in the magnetosphere by two different general physical processes. First, ULF waves can be generated in the magnetosphere's nightside sector during substorms triggered by long-period (>60 min) solar wind Alfvénic fluctuations (Rubtsov et al., 2018). This process can drive ULF waves in the magnetosphere with periods as short as 10 min. In the second mechanism, short-period (1–10 min) fluctuations of solar wind parameters (density, velocity, and dynamic pressure) can directly drive magnetospheric wave activity with similar periods, whether or not substorms occur (Kepko et al., 2002; Kepko & Spence, 2003). Herein we present evidence for the former mechanism, leaving the latter for future investigation.

The IMF conditions during the global recovery discussed above suggest that the magnetosphere was embedded in solar wind Alfvénic perturbations from 22 September onward (Figure S1 in the supporting information). To evaluate how the solar wind Alfvénic perturbations generated ULF waves during this event, we examined the ground and spacecraft ULF waves signatures that will be presented below in sections 4.1 and 4.2, respectively.

First, we identified the preferential polarization mode, since it is an important parameter for the wave-particle models used to simulate ULF wave-driven radial diffusion in the radiation belt (see, e.g., Fälthammar, 1965; Fei et al., 2006; Mann et al., 2016; Schulz & Lanzerotti, 1974; Shprits et al., 2005; Su et al., 2015). Most of the different approaches used to derive ULF wave radial diffusion coefficients (e.g., Brautigam & Albert, 2000; Elkington, 2006; Ozeke et al., 2014) employ the mode of polarization as a main parameter. Each mode contributes differently to electron acceleration (Sarris et al., 2009). Dungey (1967) used the standing Alfvén wave mode (AWM) formalism to describe ULF wave polarization modes on geomagnetic field lines. In the toroidal mode, magnetospheric shells oscillate coherently with perturbations in the azimuthal direction associated with an induced electric field in the radial direction. In the poloidal mode, magnetic field oscillations are constrained to the meridional plane, associated with an induced electric field in the azimuthal direction (Dungey, 1967; Elkington, 2006; Kivelson & Russell, 1995). In the compressional mode, all of the parameters can vary, including the field-aligned component of the magnetic field, which changes the field magnitude and both the magnetic and plasma pressures (Kivelson & Russell, 1995).

4.1. ULF Waves Activity Observed by Ground Magnetometers

Figure 3 shows the ULF wave PSD calculated by a fast Fourier transform (FFT) using observations from the IMAGE ground-based magnetometer network from 22 to 24 September. The instrument's signal was filtered using a Butterworth band-pass filter, which only allows the passage of signals within the Pc5 band (1–10 mHz). For the calculation of the power spectrum, we used the short-time FFT with a moving Hamming window of 180 min. Note that ULF wave PSD and its spatial extent gradually increased throughout this interval, that is, ULF waves reached the lowest magnetospheric L-shells at the end of the period on 24 September. At 2:00 UT on 22 September, the network observed ULF PSD mostly confined to L-shells greater than 6 R_E. At 10:00 UT, the network also observes an isolated period of ULF PSD activity in the dawnside sector that reached $L \sim 3$ R_E. After that, on 23 September the network detected significant

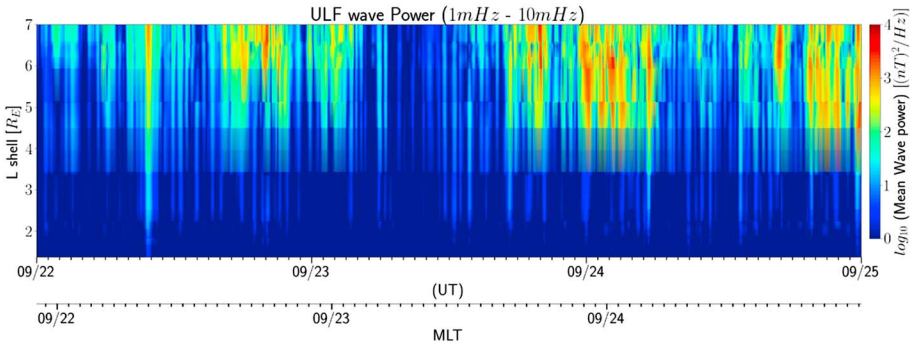

Figure 3. International Monitor for Auroral Geomagnetic Effects (IMAGE) network's ultralow-frequency (ULF) power spectral density in the 1- to 10-mHz frequency range (color scale) as a function of L-shell and time (UT = universal time and MLT = magnetic local time) from 22 to 24 September 2014.

ULF PSD in the dusk (16–19 magnetic local time [MLT]) and nightside (21–24 MLT) quadrants. Finally, at 0:00–6:00 UT and 20:00–24:00 UT on 24 September, the network observed a considerable increase in ULF PSD that penetrated inward of $L \sim 3.5\ R_E$.

From 22 to 24 September, the relativistic outer radiation belt electron fluxes (see Figures 1a and 1b) increased concurrent with the gradual enhancement in ULF PSD (Figure 3). Also, the electron flux increase reached deeper ($L \sim 4.5\ R_E$) magnetospheric L-shells, similar to the ULF wave behavior. The outer radiation belt electron flux recovered on 24 September, so we choose to investigate the ULF wave activity during this day in greater detail. Figure 4 shows the PSD from 12:00 UT on 23 September to 12:00 UT on 24 September. The intense ULF wave activity persists for 12 hr, reaching $L \sim 3.5\ R_E$.

During the 3 days analyzed (i.e., from 22 to 24 September), the ULF PSD increases preferentially in the nightside sector. This asymmetry in magnetospheric ULF wave activity can be understood by considering the IMF conditions during 24 September (Figures 1c–1e). The IMF conditions suggest enhanced reconnection/substorm activity in the magnetotail, which is confirmed by the maintenance of intense auroral activity (*AE* index ~ 1,200 nT; Figure 2e) and by the signature of Pi2 activity (Figure S2 in the supporting information). Previous work (Shiokawa et al., 2005; Wang et al., 2015) associates Pi2 signatures with Alfvénic IMF fluctuations (see Figure S1 in the supporting information). We suggest that the substorms and magnetotail reconnection play an important role in the generation and maintenance of the ULF waves.

4.2. ULF Wave Activity Observed by Spacecraft Magnetometers

We applied a Butterworth band-pass filter to the EMFISIS magnetic field and EFW electric field measurements. The ULF wave modes are characterized as fast (compressional), poloidal, and toroidal

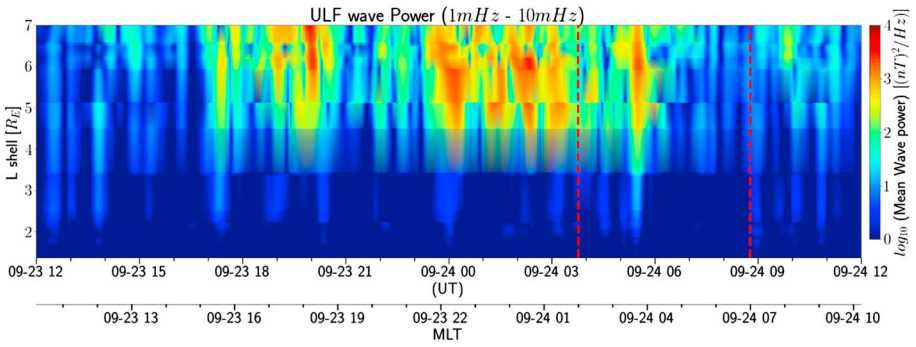

Figure 4. International Monitor for Auroral Geomagnetic Effects (IMAGE) network's ultralow-frequency (ULF) power spectral density in the 1- to 10-mHz frequency range (color scale) as a function of L-shell and time (UT = universal time and MLT = magnetic local time) between 12 noon on 23 September and 12 noon on 24 September 2014. Interval between dashed red lines represent the period of the Van Allen Probes orbit.

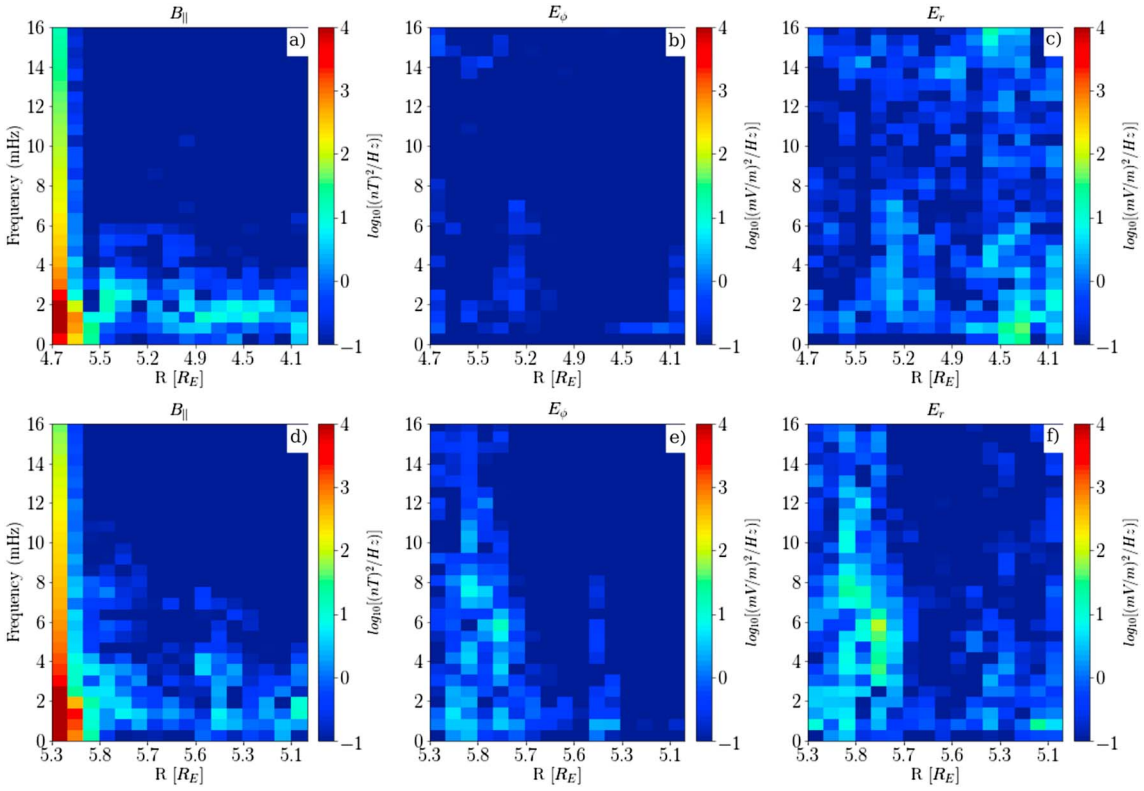

Figure 5. The ultralow-frequency power spectral density (color scale) as a function of frequency (vertical axis) and spacecraft's radial distance (horizontal axis) on 22 September 2014. Data from both the Electric and Magnetic Field Instrument Suite and Integrated Science (EMFISIS) and Electric Field and Waves (EFW) instruments on board Van Allen Probe A were used. (a–c) The first orbit and (d–f) the second orbit. The (a, d) parallel magnetic component ($B_{||}$), (b, e) azimuthal electric component (E_φ), and (c, f) radial electric component (E_r).

according to the predominant PSD component, that is, magnetic parallel ($B_{||}$), electric azimuthal (E_φ), and electric radial (E_r), respectively. To identify the polarization modes of the ULF waves, we rotate the electric and magnetic field vectors into the field-aligned coordinate system as follows: consider a location $\mathbf{s} = (x, y, z)$ in space where there is a local magnetic field vector $\mathbf{B}$, the parallel (||) direction is represented by $\mathbf{b} = \mathbf{B}/|\mathbf{B}|$, the azimuthal ($\phi$) direction is given by the cross product between $\mathbf{b}$ and the unitary position vector $\mathbf{s}/|\mathbf{s}|$, and the radial (r) direction completes the orthonormal system being positive radially outward.

Figures 5–7 present the results for the ULF waves measured by EMFISIS/EFW on 22–24 September, respectively. Each figure has six panels that show the ULF PSD calculated for the $B_{||}$ (a, d), E_φ (b, e), and E_r (c, f) components during the two of the three Van Allen Probes orbits. Comparing the PSD seen in panels (b) and (c) ((e) and (f)) of Figures 5–7, one sees that the toroidal mode dominates over the poloidal one during the whole analyzed period but most prominently on 22 September. Furthermore, panels (a) and (d), and (c) and (f) show that both the compressional and Alfvénic waves activity increased from 22 to 24 September. This observation is in an agreement with the ground-based data (see Figures 3 and 4).

On 23 and 24 September, Van Allen Probe A moved along its orbit from the nightside to the dawnside (2–7 MLT), where the spacecraft detected a substantial ULF PSD in the compressional and Alfvénic modes. By contrast, data from the IMAGE ground network (Figure 4) show intense ULF waves activity between 21:30 MLT on 23 September and 4:15 MLT on 24 September 24; that is, the MLT sector observed by the satellite covers a region where ULF waves activity is weak, except at 3:30 MLT. Thus, we simulate this event using a global magnetohydrodynamic (MHD) model (see Gombosi et al., 2004; Tóth et al., 2005; Tóth et al., 2012) to analyze the preferential ULF wave mode in the other magnetospheric MLT sectors, including those where the PSD is higher as seen by ground magnetometers.

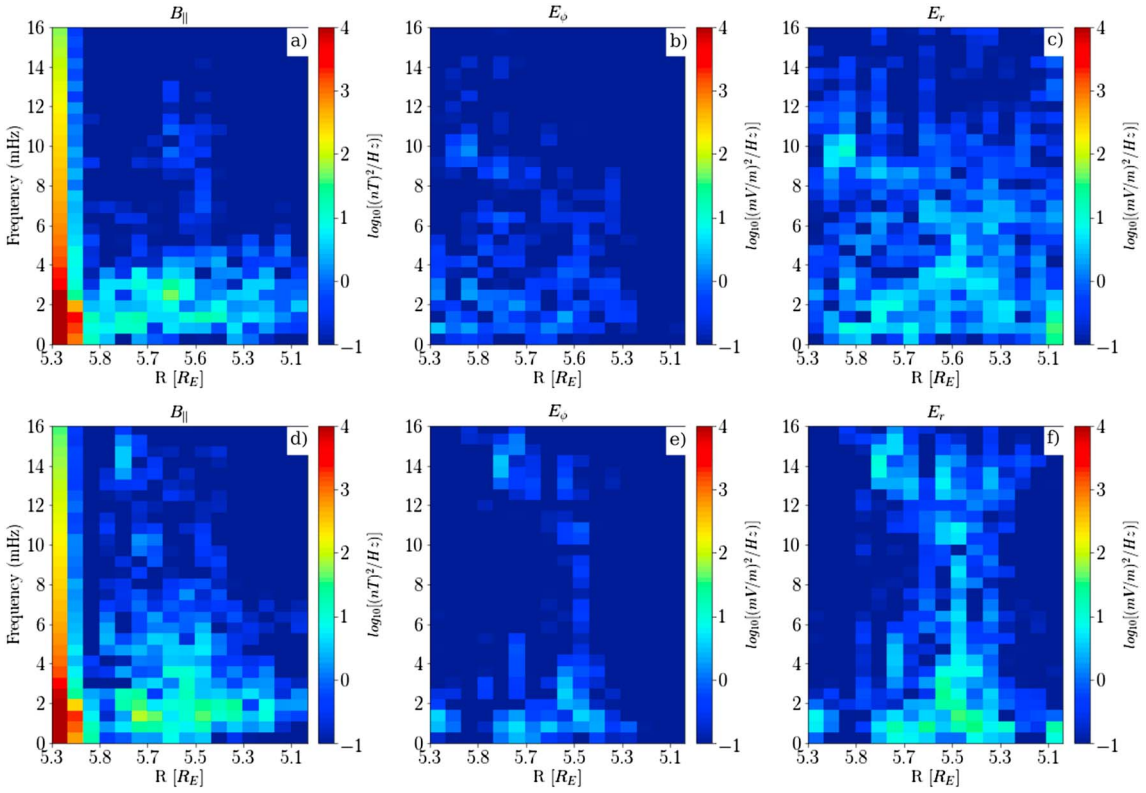

Figure 6. The ultralow-frequency power spectral density (color scale) as a function of frequency (vertical axis) and spacecraft's radial distance (horizontal axis) on 23 September 2014. Data from both the Electric and Magnetic Field Instrument Suite and Integrated Science (EMFISIS) and Electric Field and Waves (EFW) instruments on board Van Allen Probe A were used. (a–c) The first orbit and (d–f) the second orbit. The (a, d) parallel magnetic component ($B_{||}$), (b, e) azimuthal electric component (E_φ), and (c, f) radial electric component (E_r).

4.3. ULF Wave Activity as Calculated by the SWMF/BATS-R-US MHD Model

ACE observations from 22 to 24 September were used as the initial/boundary condition to model the solar wind's contribution to ULF wave activity within the magnetosphere. Electromagnetic field oscillations in the inner magnetosphere were estimated by the Space Weather Modeling Framework/Block-Adaptive-Tree Solar-Wind Roe-Type Upwind Scheme (SWMF/BATS-R-US) global MHD model (De Zeeuw et al., 2004; Gombosi et al., 2004; Powell et al., 1999; Ridley & Liemohn, 2002; Tóth et al., 2005; Tóth et al., 2012 and Wolf et al., 1977) developed at the University of Michigan in the Center for Space Environment Modeling.

The SWMF couples the different physical domains in a self-consistent mode (Tóth et al., 2012). Here we use three SWMF modules, namely, the Global Magnetosphere, Inner Magnetosphere, and Ionospheric Electrodynamics (see Alves et al., 2017). We chose a higher grid resolution of 1/8 R_E in a box surrounding the Earth with dimensions: $-7 \le x \le 7$, $-7 \le y \le 7$, and $-3 \le z \le 3$ R_E (inner boundary = ~2.5 R_E). These dimensions encompass the Van Allen belts region; thus, one can resolve electric and magnetic field fluctuations in the ULF range in this region. The MHD simulation provides a global-scale ULF PSD evaluation, including within the inner magnetosphere.

Figures 8 and 9 present the ULF PSD obtained as a result of the MHD simulation for 22 and 24 September, respectively. Figures 8 and 9 were produced in the following manner. At a given MLT, and at a given radial distance R, three time series corresponding to the modeled magnetic field $B_{||}$ component, and the modeled electric field components E_φ and E_r were obtained. These time series were acquired at $dR = 0.12$ R_E steps for each given MLT. The FFT, following Claudepierre et al. (2008), has been performed on these modeled time series, with each one spanning 24 hr of simulated time. They had a sampling rate of 1/30–33.3 mHz. The global recovery of the outer radiation belt starts on 22 September (Figures 1a, 1b, and 2a). The frequency range

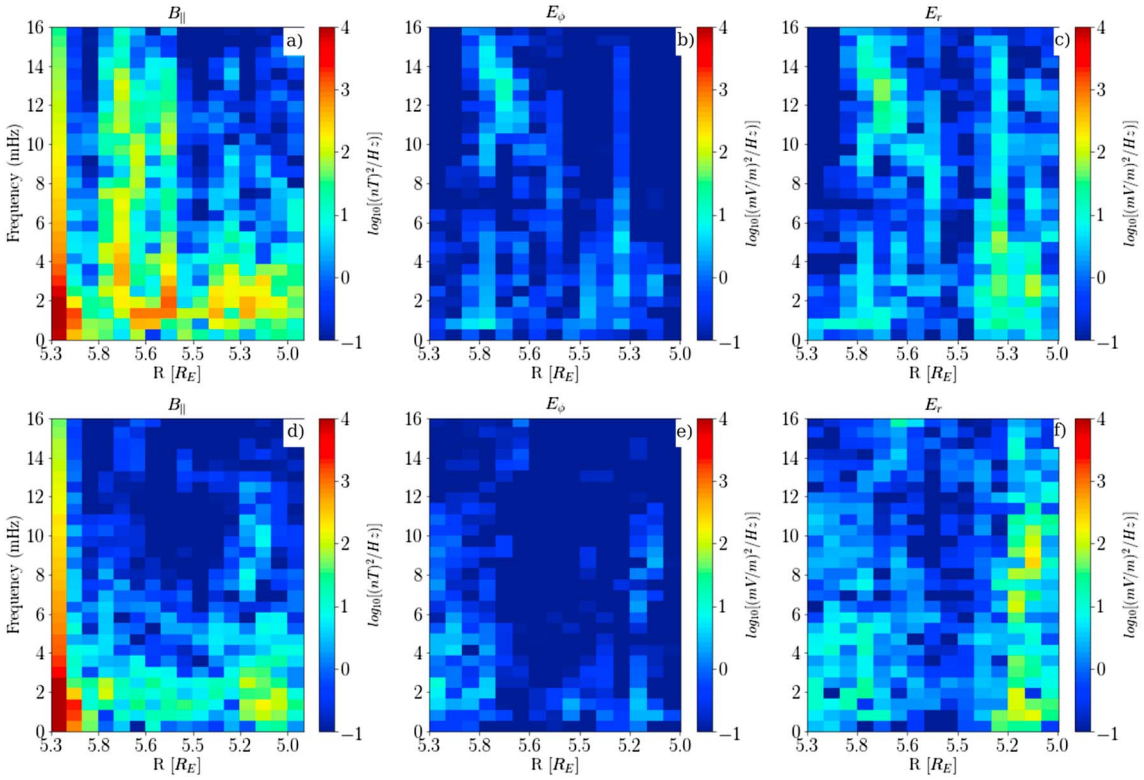

Figure 7. The ultralow-frequency power spectral density (color scale) as a function of frequency (vertical axis) and spacecraft's radial distance (horizontal axis) on 24 September 2014. Data from both the Electric and Magnetic Field Instrument Suite and Integrated Science (EMFISIS) and Electric Field and Waves (EFW) instruments on board Van Allen Probe A were used. (a–c) The first orbit and (d–f) the second orbit. The (a, d) parallel magnetic component ($B_{||}$), (b, e) azimuthal electric component (E_φ), and (c, f) radial electric component (E_r).

investigated by the simulation extends to 16.65 mHz, while the radial distance ranges from 3 to 15 R_E. Since the outer radiation belt region is typically located from the 3 to 6 R_E range, our figures and analysis are restricted to this region.

To evaluate the model reliability, we show (Figures 8d–8f and 9d–9f) the ULF wave PSD at 6 MLT for comparison with the wave activity observed by the Van Allen Probes (Figures 5a–5f and 7a–7f) at 2–7 MLT. As shown in Figures 8d and 9d, the simulation indicates enhanced compressional mode ($B_{||}$) PSD throughout the period shown. The amplitude of the toroidal mode (E_r) shown in Figure 8f predominates over that of the poloidal mode (E_φ, Figure 8e) on 22 September. Figures 9e and 9f present simulations for the poloidal and toroidal modes, respectively, on 24 September. For this period, there is no clear predominance of the toroidal mode over the poloidal mode, although near ~6 R_E, we can see a slight increase of the PSD in the toroidal mode when compared with the poloidal mode. The modeling results agree with Van Allen Probe A observations (see Figures 5 and 7) at 02:00 to 07:00 MLT, suggesting that the model also reasonably reproduces the PSD of the ULF waves at other MLTs.

The IMF *Bx* and *By* (Figure 2b) variations indicate a sector boundary crossing at 02:24 UT on 22 September, right after ACE observes very small Alfvénic fluctuations (Figures 1d, 1e, 2c, and 2d) that did not produce AWM in the dayside magnetosphere (see results in Figures 10h and 10i). Solar wind Alfvénic fluctuations increased from 23 until 24 September, ultimately resulting in magnetotail disturbances (e.g., the ground-based observations of Pi2 shown in Figure S2 of the supporting information). Disturbances like these may enhance both magnetosonic waves and AWM (Murphy et al., 2011). And in fact, on September 24 the ground-based magnetometers in the nightside sector observe a huge increase in the compressional mode (Figure 9a) with a PSD peak at ~5 R_E. The compressional mode also increases in the dawn and dusk sectors (Figures 9d and 9j). In addition, AWM perturbations are observed at dawn and dusk MLTs (Figures 11e, 11f, 11k, and 11l), midnight sector (Figures 11b and 11c), and even to a more limited degree in the dayside sector (Figures 11h and 11i).

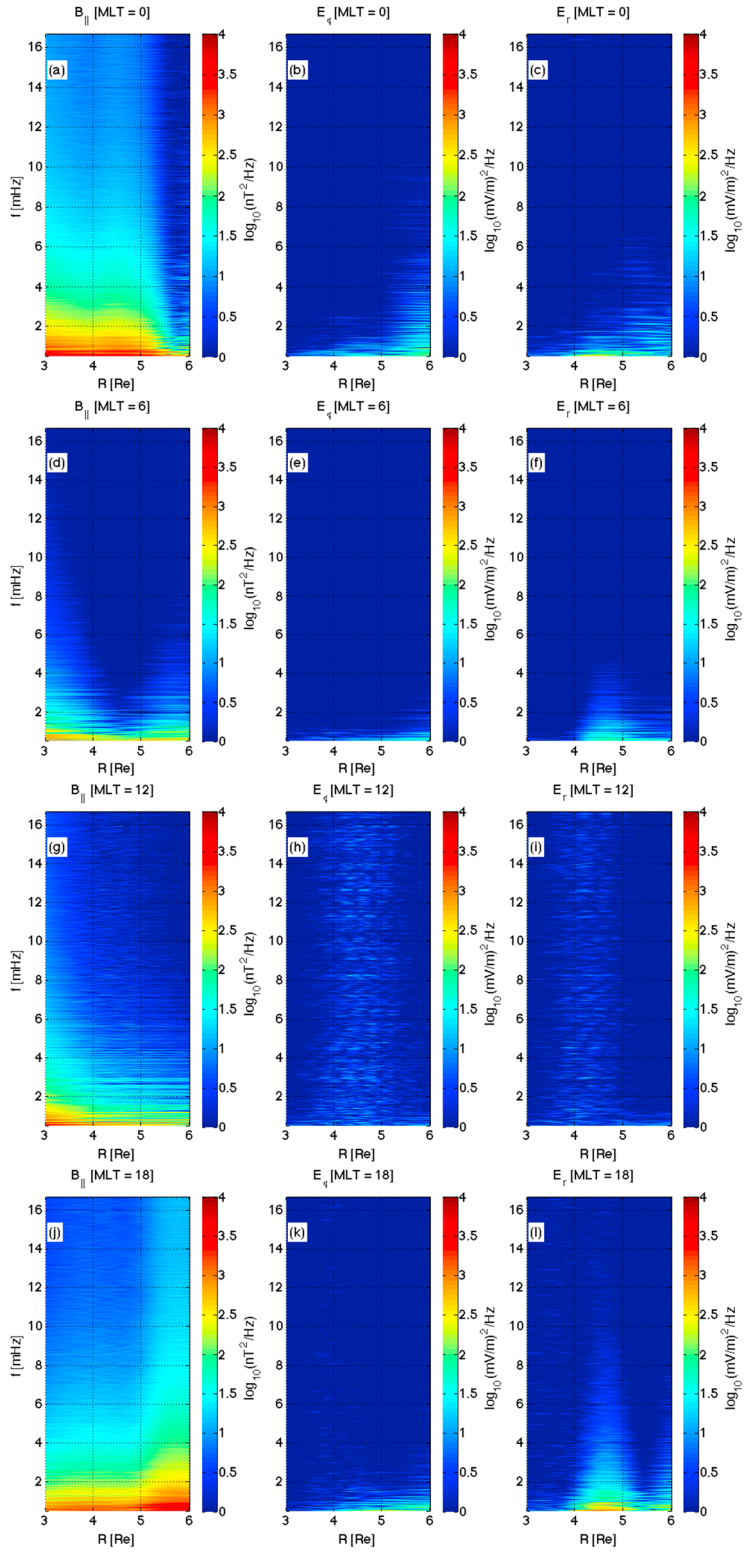

Figure 8. The ULF power spectral density (color scale) as a function of frequency (vertical axis) and radial distance (horizontal axis) simulated by the SWMF/BATS-R-US/RCM model on 22 September 2014. From top to bottom, (a–c) 00:00 MLT—midnight, (d–f) 06:00 MLT—dawnside, (g–i) 12:00 MLT—noon, and (j–l) 18:00 MLT—duskside. The (a, d, g, j) parallel magnetic component ($B_{||}$), (b, e, h, k) azimuthal electric component (E_{φ}), and (c, f, i, l) radial electric component (E_r). ULF = ultralow frequency; MLT = magnetic local time; SWMF/BATS-R-US/RCM = Space Weather Modeling Framework/Block-Adaptive-Tree Solar-Wind Roe-Type Upwind Scheme/Rice Convection Model.

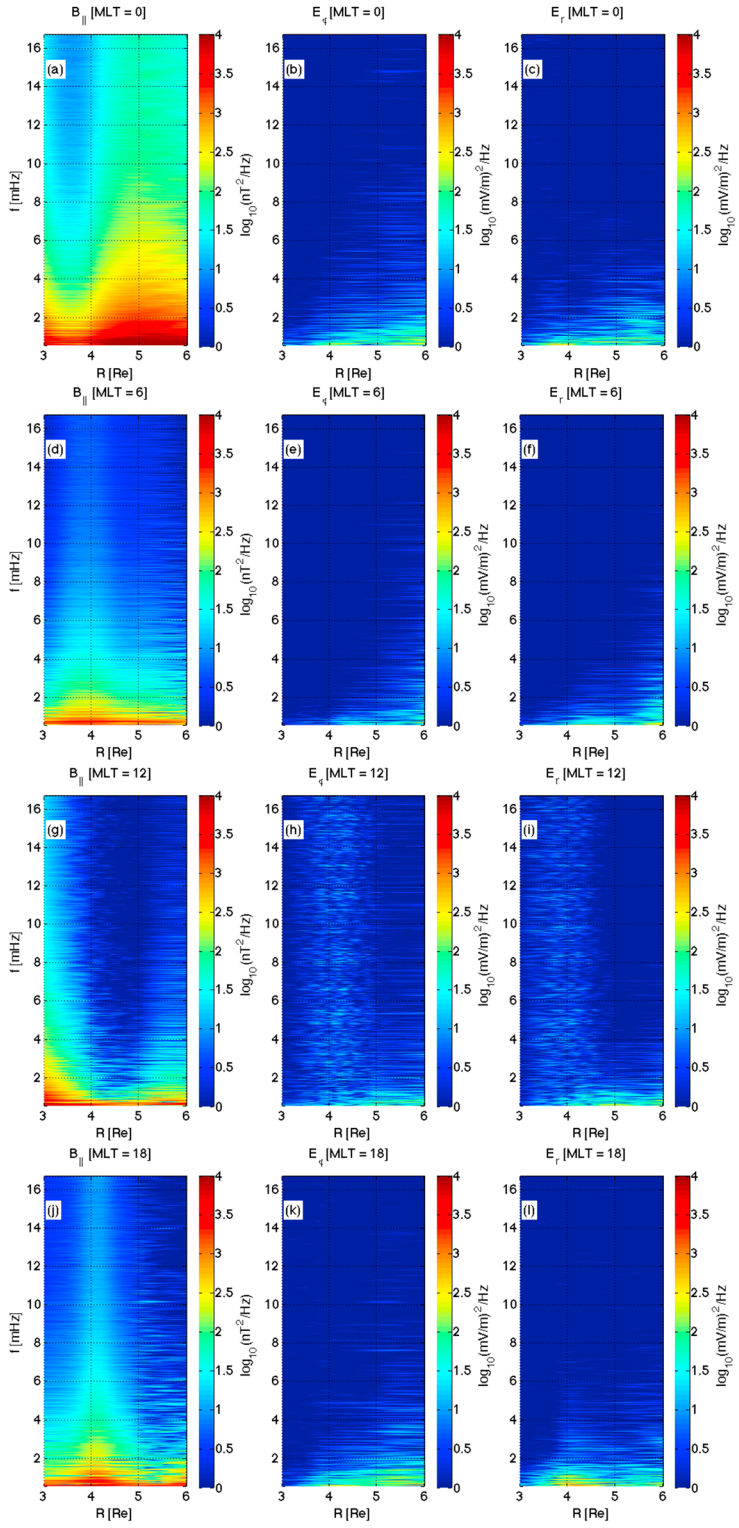

Figure 9. The ULF power spectral density (color' scale) as a function of frequency (vertical axis) and radial distance (horizontal axis) simulated by the SWMF/BATS-R-US/RCM model on 24 September 2014. From top to bottom, (a–c) 00:00 MLT—midnight, (d–f) 06:00 MLT—dawnside, (g–i) 12:00 MLT—noon, and (j–l) 18:00 MLT—duskside. The (a, d, g, j) parallel magnetic component ($B_{||}$), (b, e, h, k) azimuthal electric component (E_{φ}), and (c, f, i, l) radial electric component (E_r) are showed in the first, second and third column, respectively. ULF = ultralow frequency; MLT = magnetic local time; SWMF/BATS-R-US/RCM = Space Weather Modeling Framework/Block-Adaptive-Tree Solar-Wind Roe-Type Upwind Scheme/Rice Convection Model.

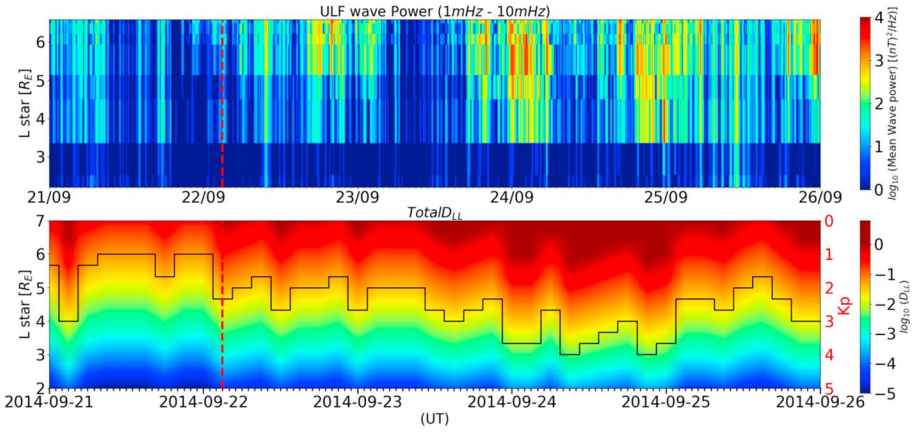

Figure 10. (top) International Monitor for Auroral Geomagnetic Effects (IMAGE) network's ultralow-frequency (ULF) power spectral density in the 1- to 10-mHz frequency range (color scale) as a function of L-shell and time from 21 to 25 September 2014. (bottom) Radial diffusion coefficient D_{LL} (color scale) as a function of L-shell (vertical axis—left) and time (horizontal axis) from 21 to 25 September 2014, estimated from the *Kp* index (vertical axis—right) data from the OMNI database with the help of the analytic expression derived by Ozeke et al. (2014). UT = universal time.

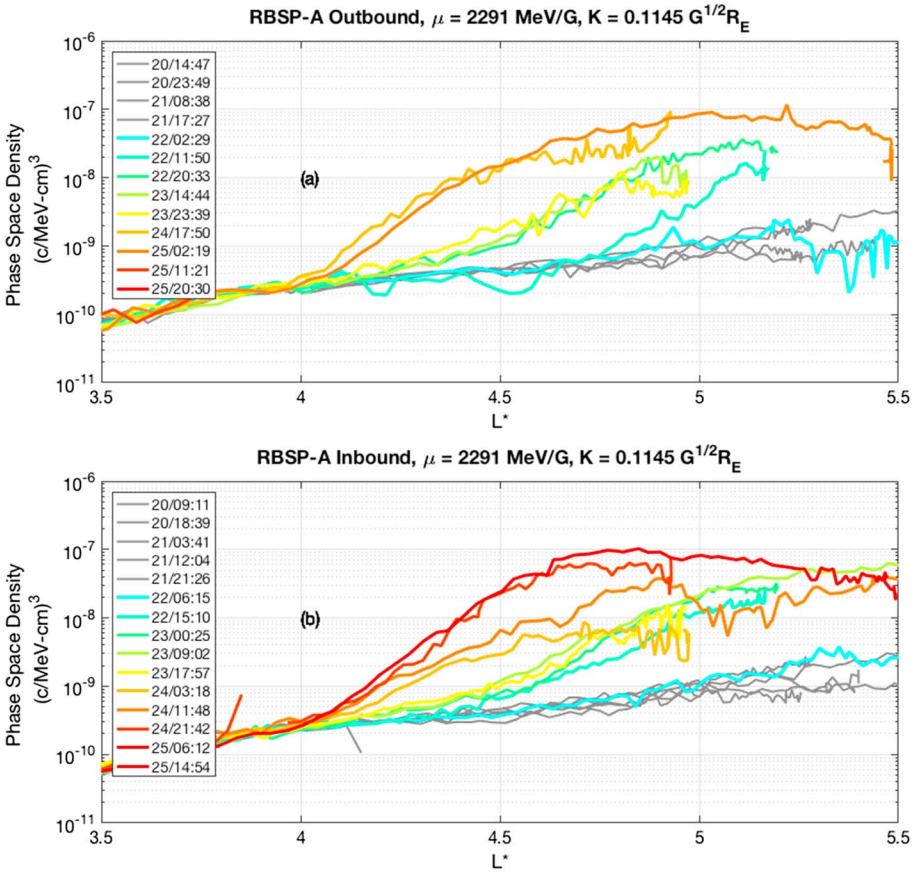

Figure 11. Time evolution of phase space density radial profiles at fixed first (μ) and second (K) adiabatic invariants for both (a) outbound and (b) inbound parts of the Radiation Belt Storm Probes (RBSP)-A orbit. The legends show the start day and time (in the dd/hh:mm format) of either the outbound or inbound portions of RBSP-A.

5. ULF Wave-Particle Interaction

The dynamic mechanisms that energize seed electrons to relativistic energies have been extensively studied (e.g., Horne & Thorne, 2003; Baker et al., 2014; Foster et al., 2014). Nevertheless, the role of ULF waves in the acceleration processes is still not well understood. Energization may occur in conjunction with inward radial diffusion driven by drift resonant interactions, as pointed out by many author (see, e.g., Elkington, 2006; Perry et al., 2005; Ukhorskiy et al., 2009). It is important to note that polarization modes can affect the efficiency of wave-particle interactions. Interactions with wave electric fields in the azimuthal direction resulting in poloidal modes are likely to be more effective to radiation belt dynamics than are interactions relying on the radial component of the electric field (Elkington, 2006).

Simulations of the drift-resonant interactions carried out by Elkington et al. (2003) and Ukhorskiy et al. (2005) show that the poloidal polarization mode is more efficient for electron acceleration than is the toroidal mode. This is because the largest component of a drifting electron's motion is in the azimuthal direction, which corresponds to the direction of the electric field in poloidal ULF pulsations.

The azimuthal particle drift motion resonantly interacts with the poloidal wave electric field when

$$\omega = m\omega_{\mathrm{d}} \tag{1}$$

where ω is the wave frequency, m is the azimuthal wavenumber, and ω_{d} is the particle drift frequency. The distribution function of particles undergoing stochastic motion in an L-shell should satisfy the radial diffusion equation

$$\frac{\partial f}{\partial t} = L^2 \frac{\partial}{\partial L}\left[\frac{D_{LL}}{L^2}\frac{\partial f}{\partial L}\right] - \frac{f}{\tau} \tag{2}$$

where f is the PhSD of electrons, and it is assumed that the first and second adiabatic invariants are conserved (Schulz & Lanzerotti, 1974). The radial diffusion coefficient and the electron lifetime are represented by D_{LL} and τ, respectively. The analytic form of the radial diffusion coefficient D_{LL} may be derived from the Hamiltonian formulation (Brizard & Chan, 2001; Fei et al., 2006). D_{LL} is the sum of the diffusion coefficient due to uncorrelated azimuthal electric field (poloidal mode) and the compressional magnetic field (fast mode) perturbations, D_{LL}^{E} and D_{LL}^{B}, respectively (Ozeke et al., 2012), that can be expressed as follows

$$D_{LL} = D_{LL}^{E} + D_{LL}^{B} \tag{3}$$

$$D_{LL}^{E} = \frac{1}{8B_E^2 R_E^2} L^6 \sum_m P_m^E(m\omega_{\mathrm{d}}) \tag{4}$$

$$D_{LL}^{B} = \frac{M^2}{8q^2\gamma^2 B^2 R_E^4} L^4 \sum_m m^2 P_m^B(m\omega_{\mathrm{d}}) \tag{5}$$

where M and γ represent the first adiabatic invariant and the relativistic correction factor, given, respectively, by

$$M = \frac{p_\perp^2 L^3}{2m_e B_E} \tag{6}$$

$$\gamma = \left(1 - {}^{v^2}\!/_{c^2}\right)^{-{}^{1}\!/_{2}} \tag{7}$$

The constants B_E, R_E,and q represent the equatorial magnetic field strength at the surface of the Earth, the Earth's radius, and the electron charge, respectively. The total speed of the electron is represented by v and the speed of light by c. The terms $P_m^E(m\omega_{\mathrm{d}})$ and $P_m^B(m\omega_{\mathrm{d}})$ represent the PSD of the electric and magnetic perturbations with azimuthal wave number, at the wave frequency, which satisfy the drift resonance condition.

5.1. ULF Wave-Driven Radiation Belt Radial Diffusion Coefficient

Radial diffusion can explain the high-energy electron flux increases in the radiation belt (Friedel et al., 2002; Li et al., 2001). Irregular fluctuations of magnetospheric electromagnetic fields on the timescales of the bounce-averaged drift period of energetic particles violate the particles' third adiabatic invariant and cause

random radial motion. An electron that moves to a lower L-shell and correspondently to a stronger magnetic field gains energy (due to conserving the transverse adiabatic invariant). Such the stochastic radial diffusion in the electrons' L-shell can increase particle flux at a given location and energy, depending on the initial distribution of particle properties and the existence of particle sources in the magnetosphere (see, e.g., Friedel et al., 2002; Li et al., 2001; Sarris et al., 2006).

The efficiency of drift-resonant ULF wave-particle interactions can be estimated employing an empirical model for the radial diffusion coefficient D_{LL} (see, e.g., Brautigam & Albert, 2000; Elkington et al., 2003; Ozeke et al., 2014). The model derived from equations 4 and 5 of Ozeke et al. (2014) describes the radial diffusion coefficients as a function of the geomagnetic index *Kp* and L-shell, but independent of the wave energy and *m* number:

$$D_{LL}^{B} = 6.22\,x\,10^{-13}L^{8}10^{-0.0327L^{2}+0.625L-0.0108K_{P}^{2}+0.499K_{P}} \tag{8}$$

$$D_{LL}^{E} = 2.16\,x\,10^{-8}L^{6}10^{0.217+0.461K_{P}} \tag{9}$$

These coefficients describe the acceleration of the electrons more efficiently than those of other empirical models because Ozeke et al. (2014) assume that all of the wave *m* values are positive (eastward propagating waves). Under symmetric drift resonance only positive wave (*m* values) can contribute to resonant interactions. Also, for frequencies above 8 mHz their assumption that the PSD at each wave *m* value varies as $\propto f^{-2}$may no longer be valid. To satisfy the drift resonance condition in this situation, the wave must have an *m* value ≥10 or the electrons must have energies ≥5 MeV.

To evaluate the ability of the ULF wave-particle interactions to produce the electron variations observed during the global recovery of the outer belt from 21 to 24 September 2014), we calculate the radial diffusion coefficient D_{LL} using equations (8) and (9). When analyzing this event, Jaynes et al. (2015) noted the important role that ULF waves could have played in the electron acceleration to multi-MeV energies. However, they did not evaluate the significance of the ULF waves. Thus, we employed observations and simulations to analyze ULF wave activity. We obtained the *Kp* index from both the OMNI database (King & Papitashvili, 2005) and BATS-R-US modeling. Figure 10 shows the gradual increase of ULF wave activity concurrent with that of the *Kp* index and corresponding D_{LL} coefficient enhancements. The red dashed line indicates the beginning of the global recovery of the outer radiation belt at several energy levels. The ULF wave PSD was calculated using observations from the IMAGE network (Figure 10, top), and D_{LL} was calculated using equations (3), (8), and (9). Figure S4 in the supporting information, shows the *Kp* index obtained from BATS-R-US modeling of D_{LL}, which agrees with the D_{LL} obtained from the ground-based database (Figure S3 in the supporting information).

The time evolution of D_{LL} throughout the repopulation period indicates the ability of ULF waves to fill several L-shells (L-shell ~5.5 R_E on 22 September and L-shell ~3.5 R_E on 24 September) in the outer radiation belt. An increase in the ULF waves PSD, *Kp* index, and also the D_{LL} radial diffusion coefficient coincided with the IMF sector boundary crossing, as indicated by the red dashed line in Figure 10. Furthermore, we observe enhancement of both D_{LL} and ULF waves in the heart of the outer radiation belt (L-shell ~3.5 R_E) when the *Kp* index reaches its maximum value for the period, that is, 4. In accordance with this, the outer radiation belt electron flux observed from the time when the sector boundary crossing was detected at L1 (Figures 1e and 2c) gradually increases at several L-shells (L-shell ~5.5 R_E on 22 September and L-shell ~3.5 R_E on 24 September).

The analytic electric field diffusion coefficient in equation (3) is more significant than is the magnetic field diffusion coefficient. Additionally, the observational and modeling results presented in section 4 show that toroidal and compressional ULF modes predominate during this event. However, a minor increase in the ULF waves in poloidal mode found in the simulation at 00:00 and 18:00 MLT contributed to the increase of D_{LL}.

6. PhSD Radial Profile

The analysis presented in the previous sections suggests that the PhSD is crucial for further understanding the role of the ULF waves on the global recovery of the relativistic electron flux observed in this radiation

belt enhancement event. PhSD is calculated as a function of quantities that are conserved under specific circumstances, for example, the three adiabatic invariants that constrain the electron motion: μ, K, and L^* parameter (Roederer, 1970). Time-dependent PhSD radial profiles as a function of L^* for fixed μ and K at regions within geosynchronous orbit can provide useful information.

PhSD data for Radiation Belt Storm Probes (RBSP)-A were obtained directly from https://www.rbsp-ect.lanl.gov/data_pub/PSD/. We use values of $\mu = 2291$ MeV/G and $K = 0.1145$ G 1/2 R_E because they optimize the coverage of L^* while limiting the equatorial PhSD to approximately 45–90° pitch angle range (see Reeves et al., 2013; Souza et al., 2017). It is important to highlight that the higher μ value chosen corresponds to electrons at energies $\gtrsim$1.5 MeV, at which the increase in the outer belt flux is observed.

Figure 11 presents the time evolution of PhSD radial profiles at fixed first (μ) and second (K) adiabatic invariants for both (a) outbound and (b) inbound parts of the RBSP-A orbit. The legends in Figure 11 show the start day and time (in the dd/hh:mm format) of either the outbound or inbound portions of RBSP-A.

The time evolution of the radial PhSD profile in the outbound regions of the Van Allen Probe A orbit shows that the gradients are almost always positive except on 25 September at 02:19 UT from L^* 5 R_E. In spite of the local peak that occurs later on during the analyzed period, we should point out another feature regarding the time evolution of the PhSD profiles that supports the idea that inward radial diffusion might be playing an important role on the electron flux recovery. Inspecting either the outbound or inbound portions of the RBSP-A orbits, particularly in the $L^* \sim 4.3$ to 5 range, one notices that as time goes by, the PhSD at fixed μ and K increases by approximately 0.5 to 1 orders of magnitude. In this L^* range the PhSD gradients are markedly positive, with no clear evidence of localized peaks, except for the 11:48 UT 24 September inbound profile, which shows a very localized ($L^* \sim 5 + -0.2$) change in the PhSD gradient sign, possibly related to spatially localized whistler mode chorus waves activity at that time (see, e.g., Jaynes et al., 2015, Figure 8). Overall, the PhSD profiles appear to undergo a shift toward lower L^* values, at least within the period of interest, which goes from the early morning hours of 22 September up to the late hours of 24 September. This shift of the PhSD profiles is characteristic of inward radial diffusion. The inbound portions of the Van Allen Probe A orbits exhibit positive gradients only until 23 September. Peaks located in the PhSD between L^* 4.5 and 5 R_E are observed for all times on 24 September. The analysis of the time evolution of the radial PhSD profiles during both outbound and inbound portions of Van Allen Probe A suggests that there are at least two mechanisms for electron acceleration in the outer radiation belt for this event, as indicated in the supporting information (Figures S5–S13), which show the PhSD at different values of μ. The first, due to radial diffusion, can occur through the interaction of ULF waves and particles, as studied in this work. The second, due to local acceleration, which may occur from the interaction of VLF waves and particles, confirms the analysis of this event performed by Jaynes et al. (2015) and discussed in section 3. In fact, Chen et al. (2007) and others show that peaks in the PhSD approximately at L^* 5.5 R_E is an indication that local acceleration may be the dominant mechanism in the repopulation of relativistic electron flux.

7. Concluding Remarks

This paper analyzed the relativistic electron flux increases generated by ULF wave-driven drift resonances during the 22–24 September 2014 period. The global flux recovery followed a ~10-day period in which the outer Van Allen belt was in quiescent state wherein fluxes of relativistic electrons were particularly low (see, e.g., Alves et al., 2016; Jaynes et al., 2015; Ozeke et al., 2017). The arrival at Earth of a high-speed stream early on 19 September preceded the electron flux enhancement. During the global electron flux recovery, both Alfvénic fluctuations in the three components of the IMF and a southward turning of the average IMF Bz component contributed to provide energy input to the Earth's inner magnetosphere via dayside reconnection, which in turn may drive enhanced substorm activity (see, e.g., Gonzalez et al., 1994). Also, it has been shown in the literature that substorm activity may induce ULF wave generation (see, e.g., James et al., 2013, 2015). While James et al. (2013) suggest that ULF waves can be driven by energy sources internal to the magnetosphere, James et al. (2015) suggest that the ULF waves can be driven by energy sources coming from both internal and external to the magnetosphere. According to James et al. (2015), the external sources can be Kelvin-Helmholtz instability on the magnetopause or solar wind buffeting. Our analysis suggests that the ULF waves observed when outer belt fluxes increased may have participated in electron acceleration via enhanced radial diffusion mechanism, as confirmed through the PhSD. The radial diffusion coefficients

(D_{LL}) obtained from the empirical model using both the observed and simulated *Kp* index show a gradual increase as a function of time, simultaneous to flux recovery. Also, their enhancement reached low L-shells. Since the electric azimuthal component is predominant in the D_{LL} coefficient, we concluded that the resonant wave-particle interaction by low-intensity poloidal wave mode detected by Van Allen Probes contributed to the repopulation of the outer radiation belt.

Acknowledgments
This work was carried out using the SWMF/BATS-R-US tools developed at The University of Michigan Center for Space Environment Modeling (CSEM) and made available through the NASA Community Coordinated Modeling Center (CCMC). We acknowledge the NASA Van Allen Probes, Harlan E. Spence (PI ECT; University of New Hampshire), John Wygant (PI EFW; University of Minnesota), and Craig Kletzing (PI EMFISIS; University of Iowa) for use of data. We acknowledge the NASA ACE satellite, Edward Stone (PI ACE; Caltech). We also acknowledge the IMAGE network, Kirsti Kauristie (PI IMAGE, Finnish Meteorological Institute). The authors acknowledge the SuperMAG PI Dr. Jesper W. Gjerloev, the whole SuperMAG team for data availability, and the website convenience for IMAGE data download. Ligia Alves da Silva is grateful for financial support from the Brazilian National Council for Scientific and Technological Development (CNPq/MCTIC: 118586/2017-3) and acknowledge the financial support from China-Brazil Joint Laboratory for Space Weather. This research was also supported by the National Natural Science Foundation of China (Nos. 41674145). Luis Eduardo Vieira thanks CNPq/MCTIC (grant 307404/2016-1). M. V. A. also thanks CNPq/MCTIC (310900/2016-6). M. G. has received support from the Natural Environment Research Council (NERC) Highlight Topic grant NE/P017185/1 (Rad-Sat). Work at NASA/GSFC was supported by the Van Allen Probes mission. All the data used are available, as follows: ECT: https://www.rbsp-ect.lanl.gov/data_pub/; EFW: http://themis.ssl.berkeley.edu/data/rbsp/efwcmds/; EMFISIS: https://emfisis.physics.uiowa.edu/Flight/; ACE: http://www.srl.caltech.edu/ACE/ASC/DATA/browse-data/; and IMAGE: http://supermag.jhuapl.edu/mag/.

References

Alves, L. R., Da Silva, L. A., Souza, V. M., Sibeck, D. G., Jauer, P. R., Vieira, L. E. A., et al. (2016). Outer radiation belt dropout dynamics following the arrival of two interplanetary coronal mass ejections. *Geophysical Research Letters*, *43*, 978–987. https://doi.org/10.1002/2015GL067066

Alves, L. R., Souza, V. M., Jauer, P. R., da Silva, L. A., Medeiros, C., Braga, C. R., et al. (2017). The role of solar wind structures in the generation of ULF waves in the inner magnetosphere. *Solar Physics*, *292*(7), 92. https://doi.org/10.1007/s11207-017-1113-4

Artemyev, A. V., Agapitov, O. V., Mourenas, D., Krasnoselskikh, V., & Zelenyi, L. M. (2013). Storm-induced energization of radiation belt electrons: Effect of wave obliquity. *Geophysical Research Letters*, *40*, 4138–4143. https://doi.org/10.1002/grl.50837

Baker, D. N., Blake, J. B., Callis, L. B., Cummings, J. R., Hovestadt, D., Kanekal, S., et al. (1994). Relativistic electron acceleration and decay time scales in the inner and outer radiation belts: SAMPEX. *Geophysical Research Letters*, *21*(6), 409–412. https://doi.org/10.1029/93GL03532

Baker, D. N., Jaynes, A. N., Li, X., Henderson, M. G., Kanekal, S. G., Reeves, G. D., et al. (2014). Gradual diffusion and punctuated phase space density enhancements of highly relativistic electrons: Van Allen Probes observations. *Geophysical Research Letters*, *41*, 1351–1358. https://doi.org/10.1002/2013GL058942

Baker, D. N., & Kanekal, S. G. (2008). Solar cycle changes, geomagnetic variations, and energetic particle properties in the inner magnetosphere. *Journal of Atmospheric and Solar-Terrestrial Physics*, *70*(2-4), 195–206, https://doi.org/10.1016/j.jastp.2007.08.031

Baker, D. N., Kanekal, S. G., Hoxie, V. C., Batiste, S., Bolton, M., Li, X., et al. (2013). The Relativistic Electron-Proton Telescope (REPT) instrument on board the Radiation Belt Storm Probes (RBSP) spacecraft: Characterization of Earth's radiation belt high-energy particle populations. *Space Science Reviews*, *179*(1–4), 337–381. https://doi.org/10.1007/s11214-012-9950-9

Baker, D. N., Li, X., Turner, N., Allen, J. H., Bargatze, L. F., Blake, J. B., et al. (1997). Recurrent geomagnetic storms and relativistic electron enhancements in the outer magnetosphere I: STP coordinated measurements. *Journal of Geophysical Research*, *102*(A7), 14,141–14,148. https://doi.org/10.1029/97JA00565

Baker, D. N., McPherron, R. L., Cayton, T. E., & Klebesadel, R. W. (1990). Linear prediction filter analysis of relativistic electron properties at 6.6 R_E. *Journal of Geophysical Research*, *95*(A9), 15,133–15,140. https://doi.org/10.1029/JA095iA09p15133

Balogh, A., Bothmer, V., Crooker, N. U., Forsyth, R. J., Gloeckler, G., Hewish, A., et al. (1999). The solar origin of corotating interaction regions and their formation in the inner heliosphere. *Space Science Reviews*, *89*(1–2), 141–178.

Belcher, J. W., & Davis, L. Jr. (1971). Large-amplitude Alfvén waves in the interplanetary medium, 2. *Journal of Geophysical Research*, *76*(16), 3534–3563. https://doi.org/10.1029/JA076i016p03534

Blake, J. B., Gussenhoven, M. S., Mullen, E. G., & Fillius, R. W. (1992). Identification of an unexpected space radiation hazard. *IEEE Transactions on Nuclear Science*, *39*(6), 1761–1764. https://doi.org/10.1109/23.211364

Bortnik, J., & Thorne, R. M. (2007). The dual role of ELF/VLF chorus waves in the acceleration and precipitation of radiation belt electrons. *Journal of Atmospheric and Solar-Terrestrial Physics*, *69*(3), 378–386. https://doi.org/10.1016/j.jastp.2006.05.030

Brautigam, D. H., & Albert, J. M. (2000). Radial diffusion analysis of outer radiation belt electrons during the October 9, 1990, magnetic storm. *Journal of Geophysical Research*, *105*(A1), 291–309. https://doi.org/10.1029/1999JA900344

Brizard, A. J., & Chan, A. A. (2001). Relativistic bounce-averaged quasilinear diffusion equation for low-frequency electromagnetic fluctuations. *Physics of Plasmas*, *8*(11), 4762–4771. https://doi.org/10.1063/1.1408623

Cahill, L. J., & Winckler, J. R. (1992). Periodic magnetopause oscillations observed with the GOES satellites on March 24, 1991. *Journal of Geophysical Research*, *97*(A6), 8239–8243. https://doi.org/10.1029/92JA00433

Claudepierre, S. G., Elkington, S. R., & Wiltberger, M. (2008). Solar wind driving of magnetospheric ULF waves: Pulsations driven by velocity shear at the magnetopause. *Journal of Geophysical Research*, *113*, A05218. https://doi.org/10.1029/2007JA012890

Chen, Y., Reeves, G. D., & Friedel, R. H. W. (2007). The energization of relativistic electrons in the outer Van Allen radiation belt. *Nature Physics*, *3*(9), 614–617.

Cranmer, S. R., & van Ballegooijen, A. A. (2005). On the generation, propagation, and reflection of Alfvén waves from the solar photosphere to the distant heliosphere. *The Astrophysical Journal Supplement Series*, *156*(2), 265–293. https://doi.org/10.1086/426507

De Zeeuw, D. L., Sazykin, S., Wolf, R., Gombosi, T., Ridley, A., & Tóth, G. (2004). Coupling of a global MHD code and an inner magnetosphere model: Initial results. *Journal of Geophysical Research*, *109*, A12219. https://doi.org/10.1029/2003JA010366

Dungey, J. W. (1967). Hydromagnetic waves. In S. Matsushita & W. H. Campbell (Eds.), *Physics of geomagnetic phenomena* (Vol. 2, pp. 913–933). New York: Academic Press.

Echer, E., Tsurutani, B. T., Gonzalez, W. D., & Kozyra, J. U. (2011). High speed stream properties and related geomagnetic activity during the whole heliosphere interval (WHI): 20 March to 16 April 2008. *Solar Physics*, *274*(1–2), 303–320.

Elkington, S. R. (2006). A review of ULF interactions with radiation belt electrons. In T. Kazue, P. J. Chi, & R. E. Denton (Eds.), *Magnetospheric ULF waves: Synthesis and new directions, Geophysical Monograph Series* (Vol. 169, pp. 177–194). Washington, DC. https://doi.org/10.1029/169GM12

Elkington, S. R., Hudson, M. K., & Chan, A. A. (1999). Acceleration of relativistic electrons via drift-resonant interaction with toroidal-mode Pc-5 ULF oscillations. *Geophysical Research Letters*, *26*(21), 3273–3276. https://doi.org/10.1029/1999GL003659

Elkington, S. R., Hudson, M. K., & Chan, A. A. (2003). Resonant acceleration and diffusion of outer zone electrons in an asymmetric geomagnetic field. *Journal of Geophysical Research*, *108*(A3), 1116. https://doi.org/10.1029/2001JA009202

Fälthammar, C.-G. (1965). Effects of time-dependent electric fields on geomagnetically trapped radiation. *Journal of Geophysical Research*, *70*(11), 2503–2516. https://doi.org/10.1029/JZ070i011p02503

Fei, Y., Chan, A. A., Elkington, S. R., & Wiltberger, M. J. (2006). Radial diffusion and MHD particle simulations of relativistic electron transport by ULF waves in the September 1998 storm. *Journal of Geophysical Research*, *111*, A12209. https://doi.org/10.1029/2005JA011211

Foster, J. C., Erickson, P. J., Baker, D. N., Claudepierre, S. G., Kletzing, C. A., Kurth, W., et al. (2014). Prompt energization of relativistic and highly relativistic electrons during a substorm interval: Van Allen Probes observations. *Geophysical Research Letters*, *41*, 20–25. https://doi.org/10.1002/2013GL058438

Friedel, R. H. W., Reeves, G. D., & Obara, T. (2002). Relativistic electron dynamics in the inner magnetosphere-a review. *Journal of Atmospheric and Solar-Terrestrial Physics*, *64*(2), 265–282. https://doi.org/10.1016/S1364-6826(01)00088-8

Goldstein, B. E., Neugebauer, M., & Smith, E. J. (1995). Alfvén waves, alpha particles, and pickup ions in the solar wind. *Geophysical Research Letters*, *22*(23), 3389–3392. https://doi.org/10.1029/95GL03182

Gombosi, T. I., Powell, K. G., de Zeeuw, D. L., Clauer, C. R., Hansen, K. C., Manchester, W. B., et al. (2004). Solution-adaptive magnetohydrodynamics for space plasmas: Sun-to-Earth simulations. *Computing in Science & Engineering*, *6*(2), 14–35. https://doi.org/10.1109/MCISE.2004.1267603

Gonzalez, W., Joselyn, J., Kamide, Y., Kroehl, H., Rostoker, G., Tsurutani, B., & Vasyliunas, V. (1994). What is a geomagnetic storm? *Journal of Geophysical Research*, *99*(A4), 5771–5792. https://doi.org/10.1029/93JA02867

Gosling, J. T. (1990). In C. T. Russell, E. R. Priest, & L. C. Lee (Eds.), *Physics of magnetic flux ropes* (pp. 343–346). AGU Geophys. Monogr.

Gurnett, D. A., & O'Brien, B. J. (1964). High-latitude geophysical studies with satellite Injun 3: 5. Very-low-frequency electromagnetic radiation. *Journal of Geophysical Research*, *69*(1), 65–89. https://doi.org/10.1029/JZ069i001p00065

Hendry, A. T., Rodger, C. J., Clilverd, M. A., Thomson, N. R., Morley, S. K., & Raita, T. (2012). Rapid radiation belt losses occurring during high-speed solar wind stream–driven storms: Importance of energetic electron precipitation. In *Dynamics of the Earth's radiation belts and inner magnetosphere, Geophysical Monograph Series* (Vol. 199, pp. 213–223). Washington, DC: American Geophysical Union. https://doi.org/10.1029/2012GM001299

Horne, R. B., & Thorne, R. M. (2003). Relativistic electron acceleration and precipitation during resonant interactions with whistler-mode chorus. *Geophysical Research Letters*, *30*(10), 1527. https://doi.org/10.1029/2003GL016973

Hundhausen, A.J. (1972). *Coronal expansion and the solar wind, Physics and chemistry in space* (Vol. 5, 238 pp.). Berlin; New York: Springer https://doi.org/10.1007/978-3-642-65414-5

Hundhausen, A. J. (1995). The solar wind. In M. G. Kivelson, & Russell, C. T. (Eds.), *Introduction to space physics* (Chap. 4) Cambridge University Press.

James, M., Yeoman, T., Mager, P., & Klimushkin, D. Y. (2013). The spatio-temporal characteristics of ULF waves driven by substorm injected particles. *Journal of Geophysical Research: Space Physics*, *118*, 1737–1749. https://doi.org/10.1002/jgra.50131

James, M. K., Yeoman, T. K., Mager, P. N., & Klimushkin, D. Y. (2015). Multiradar observations of substorm-driven ULF waves. *Journal of Geophysical Research: Space Physics*, *121*, 5213–5232. https://doi.org/10.1002/2015JA022102

Jaynes, A. N., Baker, D. N., Singer, H. J., Rodriguez, J. V., Loto'aniu, T. M., Ali, A. F., et al. (2015). Source and seed populations for relativistic electrons: Their roles in radiation belt changes. *Journal of Geophysical Research: Space Physics*, *120*, 7240–7254. https://doi.org/10.1002/2015JA021234

Kepko, L., & Spence, H. E. (2003). Observations of discrete, global magnetospheric oscillations directly driven by solar wind density variations. *Journal of Geophysical Research*, *108*(A6), 1257. https://doi.org/10.1029/2002JA009676

Kepko, L., Spence, H. E., & Singer, H. J. (2002). ULF waves in the solar wind as direct drivers of magnetospheric pulsations. *Geophysical Research Letters*, *29*(8), 1197. https://doi.org/10.1029/2001GL014405

King, J. H., & Papitashvili, N. E. (2005). Solar wind spatial scales in and comparisons of hourly Wind and ACE plasma and magnetic field data. *Journal of Geophysical Research*, *110*, A02104. https://doi.org/10.1029/2004JA010649

Kivelson, M. G., & Southwood, D. J. (1985). Charged particle behavior in low-frequency geomagnetic pulsations: 4. Compressional waves. *Journal of Geophysical Research*, *90*(A2), 1486–1486. https://doi.org/10.1029/JA090iA02p01486

Kivelson, M. J., & Russell, C. T. (1995). *Introduction to space physics, Cambridge Atmospheric and Space Science Series* (p. 568). Cambridge, UK: Cambridge University Press.

Kletzing, C. A., Kurth, W. S., Acuna, M., MacDowall, R. J., Torbert, R. B., Averkamp, T., et al. (2013). The Electric and Magnetic Field Instrument Suite and Integrated Science (EMFISIS) on RBSP. *Space Science Reviews*, *179*(1–4), 127–181. https://doi.org/10.1007/s11214-013-9993-6

Krieger, A. S., Timothy, A. F., & Roelof, E. C. (1973). A coronal hole and its identification as the source of a high velocity solar wind stream. *Solar Physics*, *29*(2), 505–525. https://doi.org/10.1007/BF00150828

Lee, D.-Y., Lyons, L. R., Kim, K. C., Baek, J.-H., Kim, K.-H., Kim, H.-J., et al. (2006). Repetitive substorms caused by Alfvénic waves of the interplanetary magnetic field during high-speed solar wind streams. *Journal of Geophysical Research*, *111*, A12214. https://doi.org/10.1029/2006JA011685

Li, W., Ma, Q., Thorne, R. M., Bortnik, J., Kletzing, C. A., Kurth, W. S., et al. (2015). Statistical properties of plasmaspheric hiss derived from Van Allen Probes data and their effects on radiation belt electron dynamics. *Journal of Geophysical Research: Space Physics*, *120*, 3393–3405. https://doi.org/10.1002/2015JA021048

Li, X., Temerin, M., Baker, D. N., Reeves, G. D., & Larson, D. (2001). Quantitative prediction of radiation belt electrons at geostationary orbit based on solar wind measurements. *Geophysical Research Letters*, *28*(9), 1887–1890. https://doi.org/10.1029/2000GL012681

MacDonald, E. A., Blum, L. W., Gary, S. P., Thomsen, M. F., & Denton, M. H. (2010). High-speed stream driven inferences of global wave distributions at geosynchronous orbit: Relevance to radiation-belt dynamics. *Proceedings of the Royal Society A: Mathematical, Physical and Engineering Sciences*, *466*(2123), 3351–3362. https://doi.org/10.1098/rspa.2010.0076

Mann, I. R., Ozeke, L. G., Murphy, K. R., Claudepierre, S. G., Turner, D. L., Baker, D. N., et al. (2016). Explaining the dynamics of the ultra-relativistic third Van Allen radiation belt. *Nature Physics*, *12*(10), 978–983. https://doi.org/10.1038/nphys3799

Mann, I. R., Wright, A. N., Mills, K. J., & Nakariakov, V. M. (1999). Excitation of magnetospheric waveguide modes by magnetosheath flows. *Journal of Geophysical Research*, *104*(A1), 333–353. https://doi.org/10.1029/1998JA900026

Mauk, B. H., Fox, N. J., Kanekal, S. G., Kessel, R. L., Sibeck, D. G., & Ukhorskiy, A. (2012). Science objectives and rationale for the radiation belt storm probes mission. *Space Science Reviews*, *179*(1-4), 3–27. https://doi.org/10.1007/s11214-012-9908-y

Morton, R. J., Tomczyk, S., & Pinto, R. (2015). Investigating Alfvénic wave propagation in coronal open-field regions. *Nature Communications*, *6*(1), 7813. https://doi.org/10.1038/ncomms8813

Murphy, K. R., Rae, I. J., Mann, I. R., Walsh, A. P., Milling, D. K., & Kale, A. (2011). The dependence of Pi2 waveforms on periodic velocity enhancements within bursty bulk flows. *Annales de Geophysique*, *29*(3), 493–509. https://doi.org/10.5194/angeo-29-493-2011

Northrop, Theodore, G., & Edward, T. (1960). Stability of the adiabatic motion of charged particles in the Earth's field. *Physical Review*, *117*(1), 215–225. https://doi.org/10.1103/PhysRev.117.215

Ogunjobi, O., Sivakumar, V., & Mtumela, Z. (2017). A comparison of outer electron radiation belt dropouts during solar wind stream interface and magnetic cloud driven storms. *Journal of Earth System Science*, *126*(4). https://doi.org/10.1007/s12040-017-0832-0

Ozeke, L. G., Mann, I. R., Murphy, K. R., Jonathan Rae, I., & Milling, D. K. (2014). Analytic expressions for ULF wave radiation belt radial diffusion coefficients. *Journal of Geophysical Research: Space Physics*, *119*, 1587–1605. https://doi.org/10.1002/2013JA019204

Ozeke, L. G., Mann, I. R., Murphy, K. R., Rae, I. J., Milling, D. K., Elkington, S. R., et al. (2012). Ulf wave derived radiation belt radial diffusion coefficients. *Journal of Geophysical Research*, *117*, A04222. https://doi.org/10.1029/2011JA017463

Ozeke, L. G., Mann, I. R., Murphy, K. R., Sibeck, D. G., & Baker, D. N. (2017). Ultra-relativistic radiation belt extinction and ULF wave radial diffusion: Modeling the September 2014 extended dropout event. *Geophysical Research Letters*, *44*, 2624–2633. https://doi.org/10.1002/2017GL072811

Paulikas, G. A., & Blake, J. B. (1979). Effects of the solar wind on magnetospheric dynamics: Energetic electrons at the synchronous orbit, in *Quantitative modeling of magnetospheric processes, Geophysical Monograph Series* (Vol. 21, pp. 180–202). Washington, DC: American Geophysical Union.

Perry, K. L., Hudson, M. K., & Elkington, S. R. (2005). Incorporating spectral characteristics of Pc5 waves into three-dimensional radiation belt modeling and the diffusion of relativistic electrons. *Journal of Geophysical Research*, *110*, A03215. https://doi.org/10.1029/2004JA010760

Potapov, A. S. (2013). ULF wave activity in high-speed streams of the solar wind: Impact on the magnetosphere. *Journal of Geophysical Research: Space Physics*, *118*, 6465–6477. https://doi.org/10.1002/2013JA019119

Powell, K. G., Roe, P. L., Linde, T. J., Gombosi, T. I., & De Zeeuw, D. L. (1999). A solution-adaptive upwind scheme for ideal magnetohydrodynamics. *Journal of Computational Physics*, *154*(2), 284–309. https://doi.org/10.1006/jcph.1999.6299

Reeves, G. D., Spence, H. E., Henderson, M. G., Morley, S. K., Friedel, R. H. W., Funsten, H. O., et al. (2013). Electron acceleration in the heart of the Van Allen radiation belts. *Science*, *341*(6149), 991–994. https://doi.org/10.1126/science.1237743

Ridley, A. J., & Liemohn, M. W. (2002). A model-derived storm time asymmetric ring current driven electric field description. *Journal of Geophysical Research*, *107*(A8), 1151. https://doi.org/10.1029/2001JA000051

Roederer, J. G. (1970). Dynamics of geomagnetically trapped radiation. In *Physics and chemistry in space* (Vol. 2). Berlin: Springer. https://doi.org/10.1007/978-3-642-49300-3

Rubtsov, A. V., Agapitov, O. V., Mager, P. N., Klimushkin, D. Y., Mager, O. V., Mozer, F. S., & Angelopoulos, V. (2018). Drift resonance of compressional ULF waves and substorm injected protons from multi-point THEMIS measurements. *Journal of Geophysical Research: Space Physics*, *123*, 9406–9419. https://doi.org/10.1029/2018JA025985

Sarris, T., Li, X., & Temerin, M. (2006). Simulating radial diffusion of energetic (MeV) electrons through a model of fluctuating electric and magnetic fields. *Annales de Geophysique*, *24*(10), 2583–2598. https://doi.org/10.5194/angeo-24-2583-2006

Sarris, T. E., Liu, W., Kabin, K., Li, X., Elkington, S. R., Ergun, R., et al. (2009). Characterization of ULF pulsations by THEMIS. *Geophysical Research Letters*, *36*, L04104. https://doi.org/10.1029/2008GL036732

Schulz, M., & Lanzerotti, L. J. (1974). *Particle diffusion in the radiation belts*. New York: Springer-Verlag. https://doi.org/10.1007/978-3-642-65675-0

Shabansky, V. P. (1971). Some processes in the magnetosphere. *Space Science Reviews*, *12*(3), 299. https://doi.org/10.1007/BF00165511–418.

Sheeley, N. R. Jr., Harvey, J. W., & Feldman, W. C. (1976). Coronal holes, solar wind streams, and recurrent geomagnetic disturbances: 1973–1976. *Solar Physics*, *49*(2), 271–278. https://doi.org/10.1007/BF00162451

Shiokawa, K., Shinohara, I., Mukai, T., Hayakawa, H., & Cheng, C. Z. (2005). Magnetic field fluctuations during substorm-associated dipolarizations in the nightside plasma sheet around $X = -10\ R_E$. *Journal of Geophysical Research*, *110*, A05212. https://doi.org/10.1029/2004JA010378

Shprits, Y. Y., Thorne, R. M., Reeves, G. D., & Friedel, R. (2005). Radial diffusion modeling with empirical lifetimes: Comparison with CRRES observations. *Annales de Geophysique*, *23*(4), 1467–1471. https://doi.org/10.5194/angeo-23-1467-2005

Souza, V. M., Lopez, R. E., Jauer, P. R., Sibeck, D. G., Pham, K., da Silva, L. A., et al. (2017). Acceleration of radiation belt electrons and the role of the average interplanetary magnetic field B_z component in high speed streams. *Journal of Geophysical Research: Space Physics*, *122*, 10,084–10,101. https://doi.org/10.1002/2017JA024187

Stone, E. C., Frandsen, A. M., Mewaldt, R. A., Christian, E. R., Margolies, D., Ormes, J. F., & Snow, F. (1998). The Advanced Composition Explorer. *Space Science Reviews*, *86*(1/4), 1–22. https://doi.org/10.1023/A:1005082526237

Su, Z., Zhu, H., Xiao, F., Zong, Q. G., Zhou, X. Z., Zheng, H., et al. (2015). Ultra-low-frequency wave-driven diffusion of radiation belt relativistic electrons. *Nature Communications*, *6*(1). https://doi.org/10.1038/ncomms10096

Summers, D., & Ma, C. (2000). A model for generating relativistic electrons in the Earth's inner magnetosphere based on gyro-resonant wave-particle interactions. *Journal of Geophysical Research*, *105*(A2), 2625–2639. https://doi.org/10.1029/1999JA900444

Summers, D., Ma, C., Meredith, N. P., Horne, R. B., Thorne, R. M., Heynderickx, D., & Anderson, R. R. (2002). Model of the energization of outer-zone electrons by whistler-mode chorus during the October 9, 1990 geomagnetic storm. *Geophysical Research Letters*, *29*(24), 2174. https://doi.org/10.1029/2002GL016039

Thorne, R. M. (2010). Radiation belt dynamics: The importance of wave-particle interactions. *Geophysical Research Letters*, *37*, L22107. https://doi.org/10.1029/2010GL044990

Thorne, R. M., Li, W., Ni, B., Ma, Q., Bortnik, J., Chen, L., et al. (2013). Rapid local acceleration of relativistic radiation-belt electrons by magnetospheric chorus. *Nature*, *504*(7480), 411–414. https://doi.org/10.1038/nature12889

Thorne, R. M., O'Brien, T. P., Shprits, Y. Y., Summers, D., & Horne, R. B. (2005). Timescale for MeV electron microburst loss during geomagnetic storms. *Journal of Geophysical Research*, *110*, A09202. https://doi.org/10.1029/2004JA010882

Tóth, G., Sokolov, I. V., Gombosi, T. I., Chesney, D. R., Clauer, C. R., De Zeeuw, D. L., et al. (2005). Space weather modeling framework: A new tool for the space science community. *Journal of Geophysical Research*, *110*, A12226. https://doi.org/10.1029/2005JA011126

Tóth, G., van der Holst, B., Sokolov, I. V., Zeeuw, D. L. D., Gombosi, T. I., Fang, F., et al. (2012). Adaptive numerical algorithms in space weather modeling. *Journal of Computational Physics*, *231*(3), 870–903. https://doi.org/10.1016/j.jcp.2011.02.006

Tsurutani, B. T., Gonzalez, W. D., Gonzalez, A. L., Tang, F., Arballo, J. K., & Okada, M. (1995). Interplanetary origin of geomagnetic activity in the declining phase of the solar cycle. *Journal of Geophysical Research*, *100*(A11), 21,717–21,733. https://doi.org/10.1029/95JA01476

Tsurutani, B. T., Gonzalez, W. D., Gonzalez, A. L. C., Guarnieri, F. L., Gopalswamy, N., Grande, M., et al. (2006). Corotating solar wind streams and recurrent geomagnetic activity: A review. *Journal of Geophysical Research*, *111*, A07S01. https://doi.org/10.1029/2005JA011273

Tu, C.-Y., & Marsch, E. (1995). MHD structures, waves and turbulence in the solar wind: Observations and theories. *Space Science Reviews*, *73*(1-2), 1–210. https://doi.org/10.1007/BF00748891

Turner, D. L., Angelopoulos, V., Li, W., Hartinger, M. D., Usanova, M., Mann, I. R., et al. (2013). On the storm-time evolution of relativistic electron phase space density in Earth's outer radiation belt. *Journal of Geophysical Research: Space Physics*, *118*, 2196–2212. https://doi.org/10.1002/jgra.50151

Ukhorskiy, A. Y., & Sitnov, M. I. (2013). Dynamics of radiation belt particles. *Space Science Reviews*, *179*(1-4), 545–578. https://doi.org/10.1007/s11214-012-9938-5

Ukhorskiy, A. Y., Sitnov, M. I., Takahashi, K., & Anderson, B. J. (2009). Radial transport of radiation belt electrons due to storm time Pc5 waves. *Annales de Geophysique*, *27*(5), 2173–2181. https://doi.org/10.5194/angeo-27-2173-2009

Ukhorskiy, A. Y., Takahashi, K., Anderson, B. J., & Korth, H. (2005). Impact of toroidal ULF waves on the outer radiation belt electrons. *Journal of Geophysical Research*, *110*, A10202. https://doi.org/10.1029/2005JA011017

Viljanen, A., & Hakkinen, L. (1997). Image magnetometer network. In M. Lockwood, M. N. Wild, & H. J. Opgenoorth (Eds.), *Satellite-ground based coordination sourcebook* (ESA SP-1198, pp. 111–117). ESA Publications.

Wang, G. Q., Ge, Y. S., Zhang, T. L., Nakamura, R., Volwerk, M., Baumjohann, W., et al. (2015). A statistical analysis of Pi2-band waves in the plasma sheet and their relation to magnetospheric drivers. *Journal of Geophysical Research: Space Physics*, *120*, 6167–6175. https://doi.org/10.1002/2014JA020753

Wolf, R. A., Harel, M., Spiro, R. W., Voigt, G.-H., Reiff, P. H., & Chen, C. K. (1977). Computer simulation of inner magnetospheric dynamics for the magnetic storm of July 29, 1977. *Journal of Geophysical Research*, *87*(A8), 5949–5962. https://doi.org/10.1029/JA087iA08p05949

Wygant, J. R., Bonnell, J. W., Goetz, K., Ergun, R. E., Mozer, F. S., Bale, S. D., et al. (2013). The Electric Field and Waves Instruments on the Radiation Belt Storm Probes mission. *Space Science Reviews*, *179*(1-4), 183–220. https://doi.org/10.1007/s11214-013-0013-7

Zhang, X.-Y., Moldwin, M. B., Steinberg, J. T., & Skoug, R. M. (2014). Alfvén waves as a possible source of long-duration, large-amplitude, and geoeffective southward IMF. *Journal of Geophysical Research: Space Physics.*, *119*, 3259–3266. https://doi.org/10.1002/2013JA019623